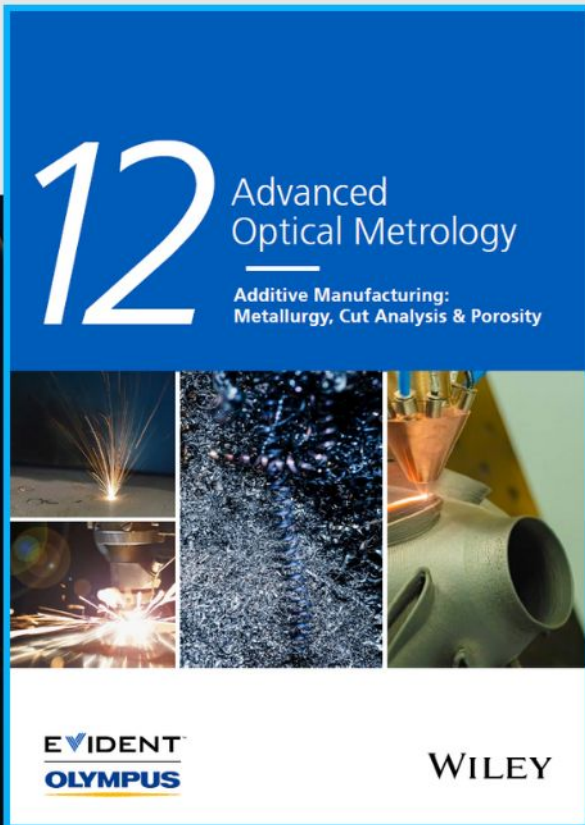




Additive Manufacturing: Metallurgy, Cut Analysis & Porosity



The latest eBook from
Advanced Optical Metrology.
Download for free.

In industry, sector after sector is moving away from conventional production methods to additive manufacturing, a technology that has been recommended for substantial research investment.

Download the latest eBook to read about the applications, trends, opportunities, and challenges around this process, and how it has been adapted to different industrial sectors.

EVIDENT
OLYMPUS

WILEY

Self-driven Electrical Stimulation Promotes Cancer Catalytic Therapy Based on Fully Conjugated Covalent Organic Framework Nanocages

Shuncheng Yao, Minjia Zheng, Shaobo Wang, Tian Huang, Zhuo Wang, Yunchao Zhao, Wei Yuan, Zhou Li, Zhong Lin Wang,* and Linlin Li*

Engineered nanozymes have been developed to catalyze the production of reactive oxygen species (ROS) for cancer therapy, but currently, the ROS generation efficiency is still far from optimistic. In this study, a human self-driven electrical stimulation enhanced catalytic system based on wearable triboelectric nanogenerator (TENG) and fully π -conjugated covalent organic framework nanocages (hCOF) for improving cancer therapy is created. The fully π -conjugated hCOF nanocage with high electron mobility under the self-generated electric field can not only rearrange the local electric field for optimizing energy utilization, but also facilitates the access of electrolytes to optimize the utilization of the electric field. With the self-powered wearable TENG, the peroxidase-like activity of hCOF increased by 2.44-fold and has electricity-responsive doxorubicin delivery capacity for enhancing the therapeutic outcomes. The high-efficient self-driven electrical stimulation enhanced nanocatalytic system provides a new optimized model for the catalytic energy supply of nanozymes.

1. Introduction

In the recent decade, great efforts have been made to carry out cancer catalytic therapy using nanozymes, in which elaborately-designed nanozymes can catalyze the generation of toxic species especially reactive oxygen species (ROS) using the tissues' local molecules as substrates.^[1] Currently, most of the developed nanozymes still have poor catalytic performance and low ROS production under the complex and variable tumor microenvironment (TME), inducing unsatisfactory therapeutic effects.^[2] Therefore, it is of fundamental and clinical importance to develop efficient methods to enhance the catalytic activity of nanozymes. More recently, the catalytic efficiency has been improved by designing nanozymes with different structures and

functions.^[3] For instance, the catalytic efficiency can be improved by designing nanocatalysts with a high degree of π -conjugation to achieve high charge transfer capacity and low charge transfer resistance, thus stabilizing the intermediate state during the catalytic reaction and transferring electrons to the intermediate state faster.^[3a,4] Therefore, new pathways to optimize electron distribution and improve electron mobility is urgently needed.

Exogenous stimuli including near-infrared light^[5], ultrasound^[6], magnetic field^[7], microwave^[8], and electric field^[9] have been utilized to promote the redox reaction for ROS production. External electric field, as a stimulus that regulates electron motion, plays an important role in reshaping the internal electrostatic field of enzymes to control catalytic reactions in terms of reactivity and selectivity.^[10] Relative to other exogenous stimuli, electric fields can cover the entire tumor tissue, avoiding the recurrence of a few cancer cells that escape from the damage.^[9] The emerging mechanical-electrical conversion technology of self-powered triboelectric nanogenerator (TENG) provides a unique opportunity for realizing a more safe, convenient, and smart nanocatalytic therapy through electrical stimulation because TENG is capable of converting mechanical energies from human motion such as heartbeat, respiration, and daily movement into electricity.^[11] Compared to conventional ways of delivering electrical stimulation, TENG with its characteristic of high voltage and low current output ensures a high degree of biosafety for in vivo applications. In addition,

S. Yao, M. Zheng, S. Wang, T. Huang, Z. Wang, Y. Zhao, Z. Li, Z. L. Wang, L. Li

Beijing Institute of Nanoenergy and Nanosystems

Chinese Academy of Sciences

Beijing 101400, P. R. China

E-mail: zhong.wang@mse.gatech.edu; lilinlin@binn.cas.cn

S. Yao, Z. Li, Z. L. Wang, L. Li

School of Nanoscience and Technology

University of Chinese Academy of Sciences

Beijing 101400, P. R. China

M. Zheng, S. Wang, T. Huang, Y. Zhao, Z. Li, Z. L. Wang, L. Li

Center on Nanoenergy Research

Guangxi University

Nanning 530004, P. R. China

W. Yuan

State Key Laboratory of Molecular Oncology

National Cancer Center/National Clinical Research Center for

Cancer/Cancer Hospital

Chinese Academy of Medical Sciences and Peking Union Medical College


Beijing 100021, P. R. China

Z. L. Wang

School of Materials Science and Engineering

Georgia Institute of Technology

Atlanta, GA 30332-0245, USA

 The ORCID identification number(s) for the author(s) of this article can be found under <https://doi.org/10.1002/adfm.202209142>.

DOI: 10.1002/adfm.202209142

TENGs with frequencies of a few hertz (Hz) can be applied directly without external energy emitters, providing a convenient route for the therapies. With this strategy, it is urgently needed to maximize the promotion effect of electrical stimulation on nanozymes with a well-designed structure.

Nanocatalysts with hollow structures can not only provide a homogeneous chemical microenvironment for catalytic reactions but also allow better access of substrates to the interior of the catalyst, especially under an electric field.^[12] Meanwhile, hollow structured nanocatalysts are capable of rearranging the local electric field, thus optimizing the utilization of electric field energy.^[13] Among different nanocatalysts as nanozymes, covalent organic frameworks (COFs) composed of light elements such as C, H, N, B, and O have the advantages of low density, high stability, and tunable porosity.^[14] In addition, due to the optional building blocks and customizable morphological features of COFs, it is possible to design and synthesize nanocatalysts with different enzymatic activities. Moreover, electronically conjugated COF can be fabricated to provide an ideal platform for studying their response to external electric fields.^[15]

In this work, we designed a human self-driven catalytic promotion system for cancer therapy by integrating a self-powered TENG with a hollow structured COF nanocage as a nanozyme. The COF nanocage (referred as hCOF) was fabricated using iron-porphyrin (TAPP-Fe) as the building block, 2,5-dihydroxyterephthalic acid (DHPA) as the linker, and zeolitic imidazolate framework-8 (ZIF-8) as the template to form a COF shell layer on the surface of ZIF-8 by π -stacking and Schiff base reaction (Figure 2a). ZIF-8 as a sacrificial template can expose carbon skeleton to facilitate π - π stacking of COF on its surface, thus enabling the better formation of COF shell.^[16] Moreover, ZIF-8 can be selectively removed in a weakly acidic media to generate a hollow COF structure. The rationally designed hCOF not only has the advantages of the previously reported COF nanocatalysts,^[3a] but also has the following advantages when cooperating with the electric field stimulation provided by TENG. First, the hollow structure of hCOF is beneficial to exposure of active sites of atomically dispersed iron to catalyze the production of hydroxyl radicals ($\cdot\text{OH}$) from H_2O_2 , namely peroxidase (POD)-like activity.^[3a,17] Second, the hollow and fully conjugated structure not only facilitates the entry of electrolytes^[18] and improves the sensitivity of nanocatalysts to external electric fields, but also enhances the conversion of electric field energy to facilitate catalytic reactions. Third, the hollow structure is capable of rearranging the local electric field to optimize the promotion effect of the stimulus.^[13] Forth, hCOF with a hollow and porous structure can act as an efficient drug carrier for further improving the therapeutic outcome through a combination effect.^[19] Thus, under the human self-generated electric field provided by a wearable TENG, the system can realize a maximum cancer therapeutic outcome.

2. Results and Discussion

2.1. Synthesis and Characterizations

The hollow COF nanocage hCOF was fabricated using ZIF-8 as the supporting template for COF coating (Figure 1). The carbon skeleton of ZIF-8 can provide π - π stacking substrate for

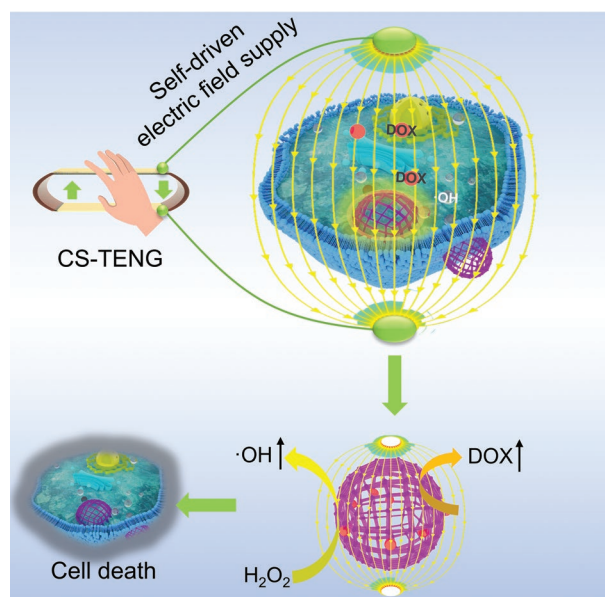


Figure 1. Schematic diagram of a human self-driven electrical stimulation enhanced catalytic system for cancer therapy based on wearable triboelectric nanogenerator (CS-TENG) and fully π -conjugated covalent organic framework nanocages (hCOF) loaded with doxorubicin (DOX).

layer-by-layer coating of the organic covalent structure to form core-shell structured COF@ZIF-8. The subsequent etching of the core ZIF-8 in mildly acidic media resulted in the formation of hCOF (Figure 2a). From the transmission electron microscope (TEM) and scanning electron microscope (SEM) (Figure 2b; Figure S1, Supporting Information) images, the core-shell structured COF@ZIF-8 had a nearly spherical morphology with a relatively uniform size (diameter of ≈ 200 nm). From the SEM and high-resolution TEM (HR-TEM) images, the resultant hCOF had a spherical and hollow structure with a diameter of ≈ 240 nm and shell thickness of ≈ 25 nm (Figure 2b,c; Figure S1, Supporting Information). The energy dispersive spectroscopy (EDS) elemental mapping images of hCOF showed the uniform distribution of Fe active sites and their coordinated N on the shell (Figure 2c), which was conducive to the catalytic reaction. The X-ray photoelectron spectroscopy (XPS) of Fe 2p can be deconvoluted into two peaks centered at ≈ 710.0 and 713.0 eV, corresponding to Fe^{3+} and Fe^{3+} , respectively (Figure 2d). From the N 1s spectrum of hCOF, the peaks centered at ≈ 400.0 eV correspond to C=N groups, proving the formation of the organic covalent structure via Schiff-base reaction (Figure 2e). The fitting peaks of imine bonds for ZIF-8 (399.7 eV) and COF@ZIF-8 (399.8 eV) had shifted location and changed intensity, which was mainly caused by the presence of ZIF-8. From the Fourier transform infrared (FT-IR) spectrum of hCOF (Figure 2f), the stretching peak of C=N at 1610 cm^{-1} , and the disappeared peak of C=O at 1681 cm^{-1} and C-N at 1168 cm^{-1} also proved the existence of imine bonds and the removal of ZIF-8. In the X-ray diffraction (XRD) pattern of hCOF (Figure 2g), the diffraction peak at 73° corresponding to (100) plane of ZIF-8 almost disappeared, and the weak diffraction peak at 8.8° corresponded to (020) plane of hCOF, illustrating that hCOF mainly existed in an amorphous form. From N_2 adsorption-desorption isotherms at 77 K, ZIF-8,

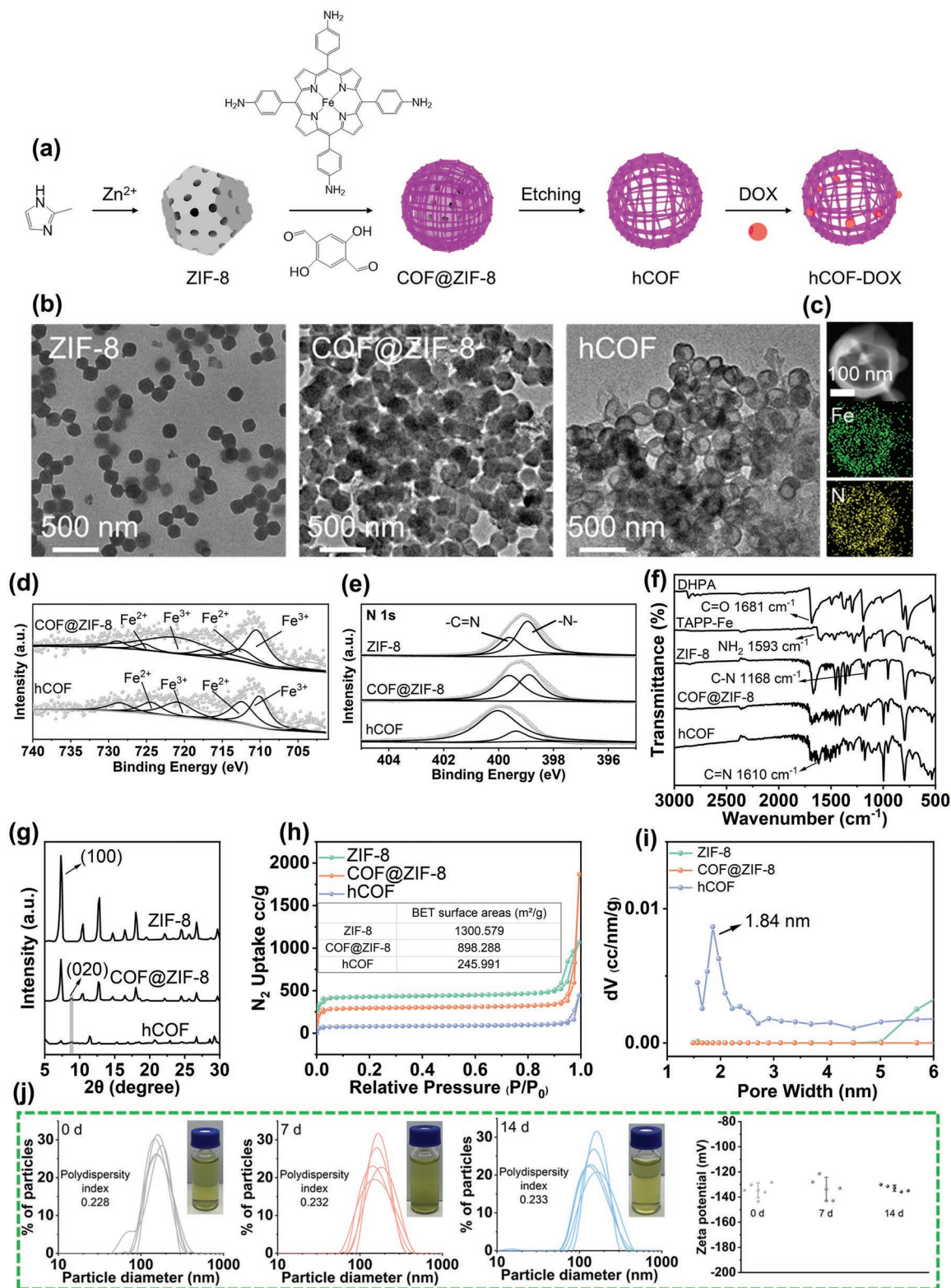


Figure 2. Preparation diagram and characterizations of hCOF. a) Schematic representation of preparing hCOF. b) TEM image of ZIF-8, COF@ZIF-8, and hCOF. c) The energy dispersive spectroscopy (EDS) element mapping of hCOF: Fe (green), and N (yellow). d) High-resolution Fe 2p XPS spectra of COF@ZIF-8 and hCOF. e) High-resolution N 1s XPS spectra of ZIF-8, COF@ZIF-8, and hCOF. f) FT-IR spectra of DHPA, TAPP-Fe, ZIF-8, COF@ZIF-8, and hCOF. g) XRD patterns of ZIF-8, hCOF, and COF@ZIF-8 (The gray region indicates the presence of COF crystalline peaks). h) N₂ adsorption-desorption isotherms of ZIF-8, COF@ZIF-8, and hCOF at 77 K. Inset is their BET surface area. i) Pore size distribution of ZIF-8, COF@ZIF-8, and hCOF. j) Hydrodynamic diameter and Zeta potential of hCOF at 0, 7, and 14 d of dispersion in aqueous solution. The insets are optical pictures of the aqueous hCOF suspensions.

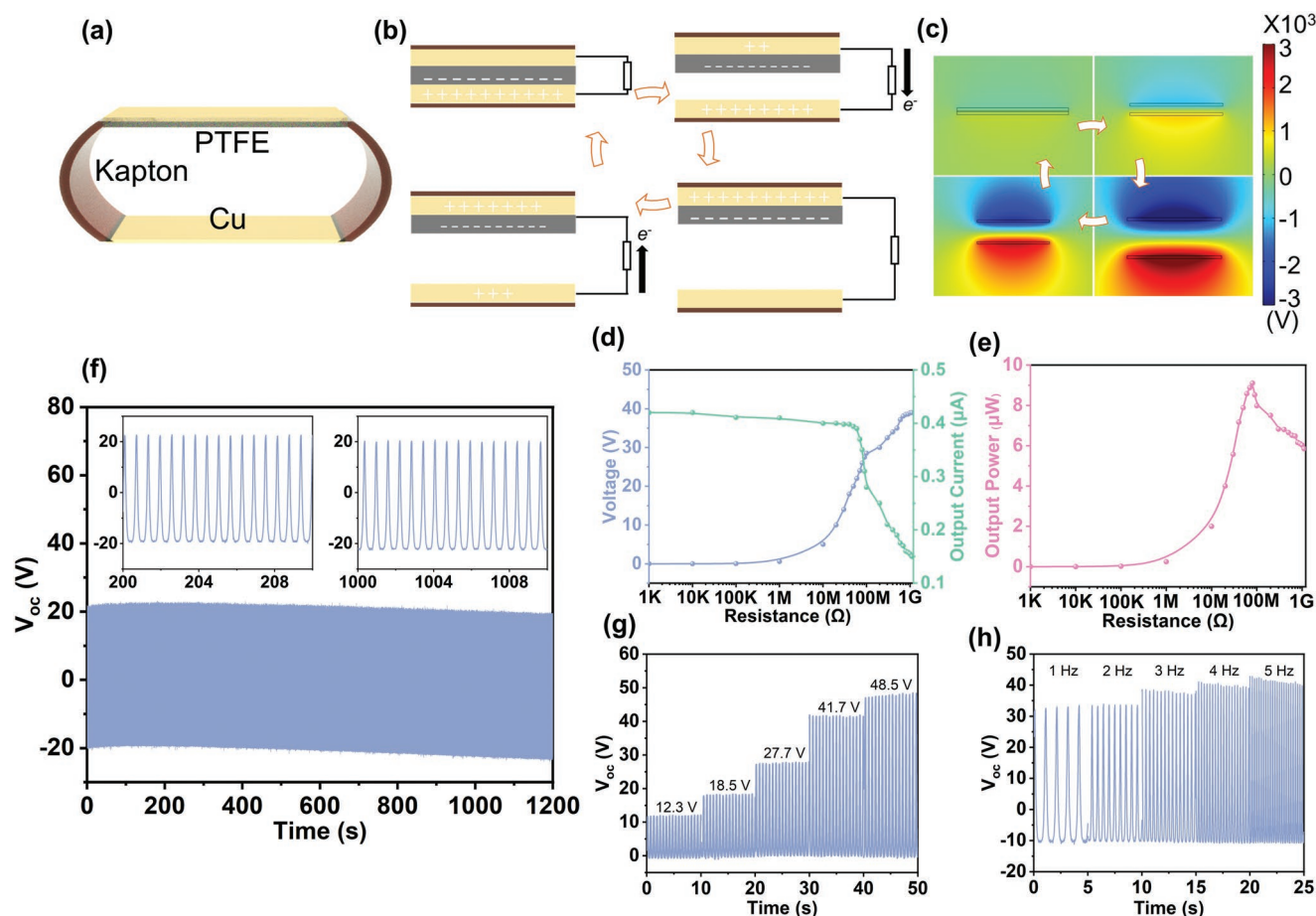


Figure 3. Fabrication and output performance of CS-TENG. a) Schematic fabrication of CS-TENG. b) A cycle of the electricity generation process of CS-TENG. c) Finite element simulation via COMSOL for analyzing the potential distribution during a contact-separation cycle. d) The output current and voltage with the resistance of external loads. e) The output power with the resistance of the external loads. f) V_{oc} output stability of CS-TENG within 600 s. Inset shows V_{oc} within 10 s. g,h) Output at different voltages and different frequencies.

COF@ZIF-8, and hCOF had typical I-type nitrogen absorption-desorption curve with Brunauer-Emmett-Teller (BET) surface area of 1300.579, 898.288, and 245.991 $\text{m}^2 \text{g}^{-1}$, respectively (Figure 2h). The decreased specific surface area of hCOF relative to ZIF-8 and COF@ZIF-8 was due to the removal of highly porous ZIF-8. The average pore diameter of hCOF was 1.84 nm (Figure 2i). These results suggested that micropores of hCOF appeared after the removal of ZIF-8. The high specific surface area and porous structure of hCOF were advantageous for drug loading and release when using it as a drug carrier. The removal of ZIF-8 did not induce the obvious change in Zeta potential and hydrodynamic size of the resultant hCOF (Figure S4, Supporting Information). In addition, hCOF had high stability in an aqueous solution. During the 14-day dispersion in an aqueous solution, the particle diameter and zeta potential were almost unchanged, demonstrating its high stability (Figure 2j).

2.2. Fabrication and Output Performance of TENG

To provide a self-driven electrical stimulation, a wearable contact-separation mode TENG (CS-TENG) driven by a human

was fabricated. The CS-TENG was composed of an upper Cu film electrode, a lower Cu film electrode, and elastic supports (30 μm Kapton film) on both sides (Figure 3a). The 30 μm poly (tetrafluoroethylene) (PTFE) film was used as the negative friction layer. A working cycle of CS-TENG is shown in Figure 3b. When the PTFE film (with a positive charge) touches the lower Cu electrode (with a negative charge), positive and negative polarities are generated on the PTFE and Cu, respectively, through contact electrification. The positive charge accumulated on the PTFE film effectively shields the negative charge on the Cu electrode. When the PTFE has moved away from the Cu electrode, the accumulated positive charge can be released through the Cu electrode, generating a current. When the PTFE moves in the opposite direction, the accumulated positive charge flows in the opposite direction through the Cu electrode. In this way, the accumulated charge moves back and forth, generating a continuous AC voltage and current. The potential distribution of CS-TENG during a working cycle was calculated using the finite element model (FEM) of COMSOL, and the result showed the as-deduced trend (Figure 3c). The CS-TENG with a contact area of $6 \times 6 \text{ cm}$ was worn on the arm of a student volunteer, and its output performance during

finger tapping was tested. When the finger tapped CS-TENG at a frequency of ≈ 1.6 Hz, the short-circuit current (I_{sc}) reached $0.35 \mu\text{A}$, and the peak open-circuit voltage (V_{oc}) reached 40 V (Figure S5, Supporting Information). As the load resistance increased, the corresponding current decreased and the voltage increased (Figure 3d). When the matching resistance was $80 \text{ M}\Omega$, the maximum power generated by CS-TENG reached $9.1 \mu\text{W}$, corresponding to a power density of 3.64 mW m^{-2} (Figure 3e). After ≈ 2000 friction cycles within 1200 s, the V_{oc} value still remained stable at 40 V (Figure 3f), indicating that CS-TENG had excellent stability. Moreover, the output V_{oc} can be tuned in the range of 10 – 50 V by applying different mechanical forces (Figure 3g). When the frequency changed within the range of 1 – 5 Hz, the output was almost constant (Figure 3h).

2.3. Mechanism and Performance of Nanozyme Catalysis

Subsequently, we studied the catalytic activities of hCOF nanozyme stimulated by the human autogenous electric field with the assistance of CS-TENG. The reaction system catalyzed by hCOF nanozyme in Tanswell 24-well plate was connected with CS-TENG driven by human fingers (Figure 4a). For detecting the effect of electric field on POD-like activity of hCOF to generate $\cdot\text{OH}$, 3,3',5,5'-tetramethylbenzidine (TMB) as a colorimetric substrate (Figure 4b), and electron spin resonance (ESR) spectra using 2-picoline-N-oxide (DMPO) as the specific trapping agent (Figure 4c) were applied to detect OH. The pH value of the dispersion media was 6.5 , which was similar to that in TME. Without any nanoparticles in the media, the OH production by decomposing H_2O_2 was almost negligible, even with the exerting of electric field. Without an electric field, the POD-like activity of hCOF was 1.5 times higher than that of COF@ZIF-8 (Figure S6 and Table S2, Supporting Information) (Take the V_{max} as the standard). When the self-generated electric field (30 V, 1.6 Hz) was applied, the POD-like activity of hCOF was significantly increased by 2.44 -fold; meanwhile, the POD-like activity of hCOF was 1.69 times higher than that of COF@ZIF-8 under electrical stimulation of the same condition. With the increase in electrical voltage and frequency of CS-TENG and decrease in pH value of dispersion media, the $\cdot\text{OH}$ production was also increased (Figure 4d). Under the self-generated electric field, the improvement in the catalytic performance of hCOF nanozyme can be mainly attributed to the high electron mobility of the fully π -conjugated organic covalent and hollow structure. As evidence, electrochemical impedance spectroscopy results (Figure 4e) showed that the impedance value significantly decreased after the formation of the fully π -conjugated COF (for COF@ZIF-8 relative to ZIF-8), and further decreased after the removal of ZIF-8 (for hCOF). Cyclic voltammetry (CV) was used to reveal the changes in the catalytic redox reaction of hCOF in the presence of an electric field under the simulated TME condition (pH 6.5 , 100×10^{-6} M H_2O_2) (Figure 4f). After the formation of the hollow structure, the current of hCOF increased significantly at -0.65 V, which was attributed to its redox reaction with H_2O_2 .^[20] Meanwhile, the current of hCOF at -0.65 V is 5.17 times higher than that of COF@ZIF-8. Moreover, the results of photocurrent showed that a significant enhancement in photocurrent occurred after

the formation of the hollow structure (hCOF relative to COF@ZIF-8) (Figure 4g). It was due to that the hollow and fully conjugated structure was beneficial to the entry of electrolytes and electron mobility. Moreover, it was deduced that the fully conjugated hCOF has a lower electron transfer resistance and more favorable electron transfer near the Fe active center,^[21] thereby greatly improving the POD-like activity.

To further confirm the reason for the increased POD-like activity of hCOF under the electric field, an electrostatic 2D simulation was carried out by COMSOL to calculate the energy density of hCOF's surface (Figure 4h). In the simulation with an ideal environment, under the applied voltage of 30 and 60 V, the surface of the fully π -conjugated hCOF has obvious energy accumulation, and the energy densities reach 2×10^{-5} and $6 \times 10^{-5} \text{ J m}^{-3}$ under 30 and 60 V, respectively. The energy accumulation will further promote electron migration and electron-mediated energy transfer.

In addition, the porous structure and high BET surface area of hCOF also showed advantages for effective drug loading.^[22] The drug loading efficiency of hCOF for DOX (denoted as hCOF-DOX) was 10.2% (Figure S7, Supporting Information). Interestingly, it showed stimulus-responsive drug release behavior under the autogenous electric field (Figure 4i). The experimental results showed that under the CS-TENG-enabled electric field with the fixed frequency of 1.6 Hz, pulse number of 288 , and one cycle time of 3 min, 15.3 , 18.8 , 24.4 , 29.7 , 33.8 , and 34.2% of the loaded DOX was cumulatively released from hCOF-DOX for 1 to 6 cycles of stimulation during 72 h, respectively. It was found that the DOX release with or without electrical stimulation almost reached a plateau within 48 h. After 48 h, electrical stimulation did not significantly improve drug release. At 72 h, the cumulative DOX release rate was 34.3% in the electrical stimulation group, whereas it was only 19.35% in the control group without electrical stimulation. The reason for the electrical stimulation fastened drug release may be due to the alteration of electrostatic interaction or hydrogen bonding between the drug molecules and hCOF under the action of an electric field.^[23] Therefore, the self-generated electric field can not only significantly improve the POD-like activity of hCOF but also act as an efficient stimulus for drug release to improve local drug delivery and accumulation. In addition, to verify whether the drug molecule release was influenced by other factors, we detected drug release under different H_2O_2 concentrations that influenced hCOF catalysis. The experimental results showed that the release of drug molecules decreased slightly with increasing H_2O_2 concentrations (0 – 100×10^{-6} M) (Figure S8, Supporting Information), which might be attributed to the interaction between H_2O_2 and DOX, which leads to a decrease in DOX absorption values (Figure S9, Supporting Information).

2.4. In Vitro Cancer Therapy

On the premise that the autogenous electric field improved the catalytic activities and drug delivery of hCOF-DOX, we further investigated the cancer therapeutic effect of hCOF-DOX under the autogenous electric field. First, we confirmed that hCOF had high cytocompatibility with normal cells. After treatment with $600 \mu\text{g mL}^{-1}$ of hCOF for 24 h, the viability of mouse NIH-3T3

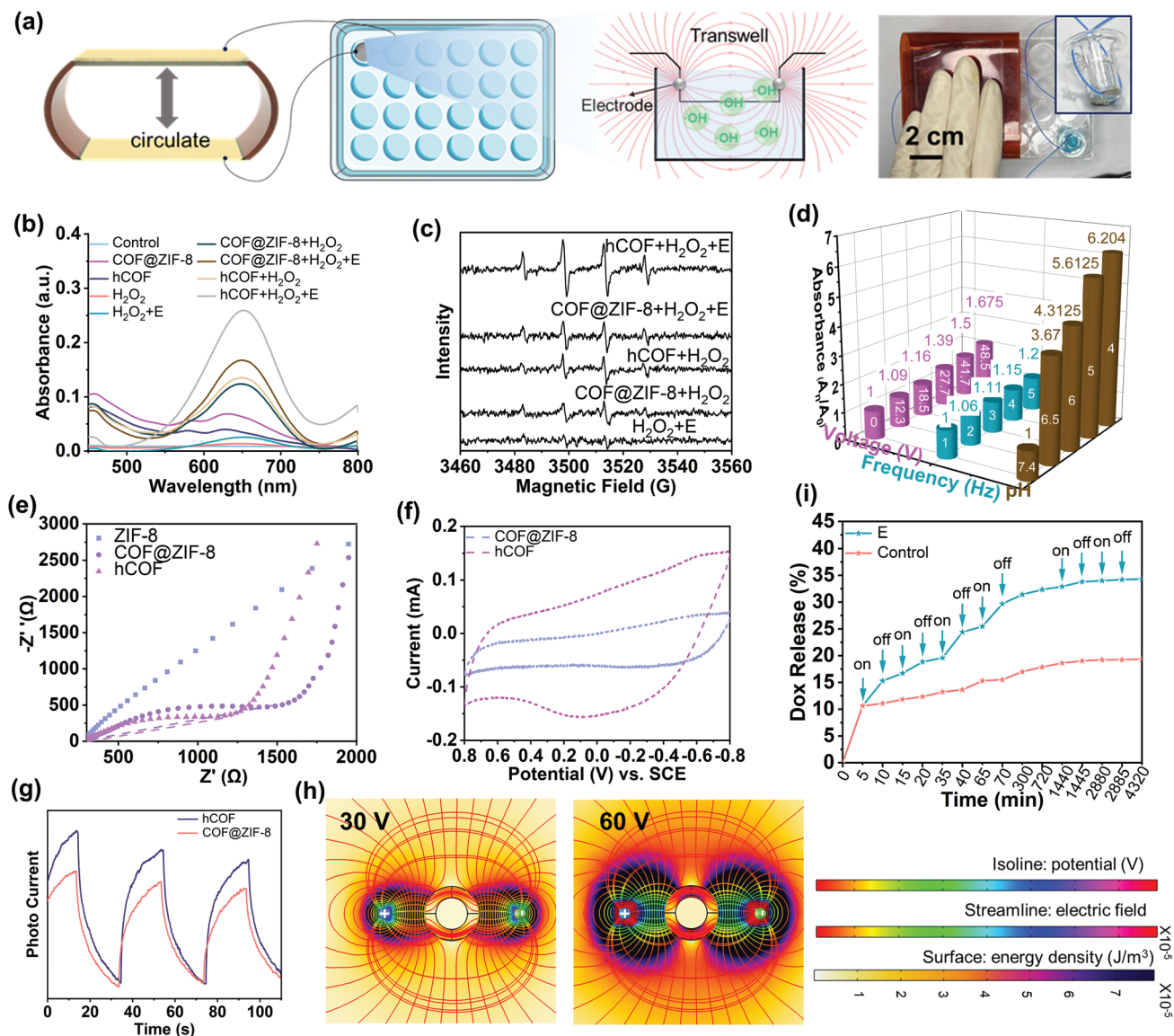


Figure 4. Catalytic and drug release properties of hCOF. a) Schematic illustration and optical photograph of the experimental design for CS-TENG-promoted catalysis of hCOF. b) POD-like activity of E, hCOF, hCOF+E, COF@ZIF-8, and COF@ZIF-8+E in pH 6.5 PBS with or without the addition of H₂O₂ (100×10^{-6} M). c) ESR spectra showing ·OH generation of COF@ZIF-8, COF@ZIF-8+E, hCOF, hCOF+E, and E with H₂O₂ (100×10^{-6} M) using DMPO as the trapping agent. d) POD-like activities of hCOF ($60 \mu\text{g mL}^{-1}$) with 100×10^{-6} M H₂O₂ at different pH values (4, 5, 6, 6.5, and 7.4), TENG voltages (0, 10, 20, 30, 40, and 50 V) and frequencies (1, 2, 3, 4, and 5 Hz). (e) EIS Nyquist plots for ZIF-8, COF@ZIF-8, and hCOF. f) Cyclic voltammograms of hCOF and COF@ZIF-8 with the addition of H₂O₂. The medium was pH 6.5 PBS of 0.2 M. g) Photocurrent of hCOF and COF@ZIF-8. h) Electrostatic 2D simulation by COMSOL of the electric field distribution, potential distribution, and energy density distribution on hCOF, under the electrical voltage of 30 and 60 V. i) Drug release behavior of hCOF-DOX with or without electric field stimulation. Electricity is shortened as E in some diagrams due to limited space.

fibroblasts was still as high as 90% (Figure 5a). The antitumor effect was evaluated on 4T1 mouse breast cancer cells with high malignancy (Figure 5b). The electric field stimulation enabled by CS-TENG (3 min, 288 pulses) was imposed on the cells grown on the cell culture plates. The results showed a $\approx 100\%$ cell survival rate with electric field stimulation alone (30 V, 1.6 Hz; Group G1 in figures), indicating that electric field stimulation did not influence cell activity. Meanwhile, 100×10^{-6} M H₂O₂ (Group G3), H₂O₂+E (Group G4), and hCOF (Group G5)

all had low cell killing ability (cell survival $>60\%$). In contrast, hCOF+H₂O₂ (Group G6) and hCOF-DOX+H₂O₂ (Group G7) decreased the cell survival rate to 44.3% and 41.6%, respectively, which was due to the addition of H₂O₂ to simulate TME condition increased the ·OH generation catalyzed by hCOF.

With the combined action of H₂O₂ and electricity, the cell survival with the treatment of hCOF ($150 \mu\text{g mL}^{-1}$) and hCOF-DOX ($150 \mu\text{g mL}^{-1}$) further decreased to 26% and 19%, respectively. The reason for the different killing effects between the

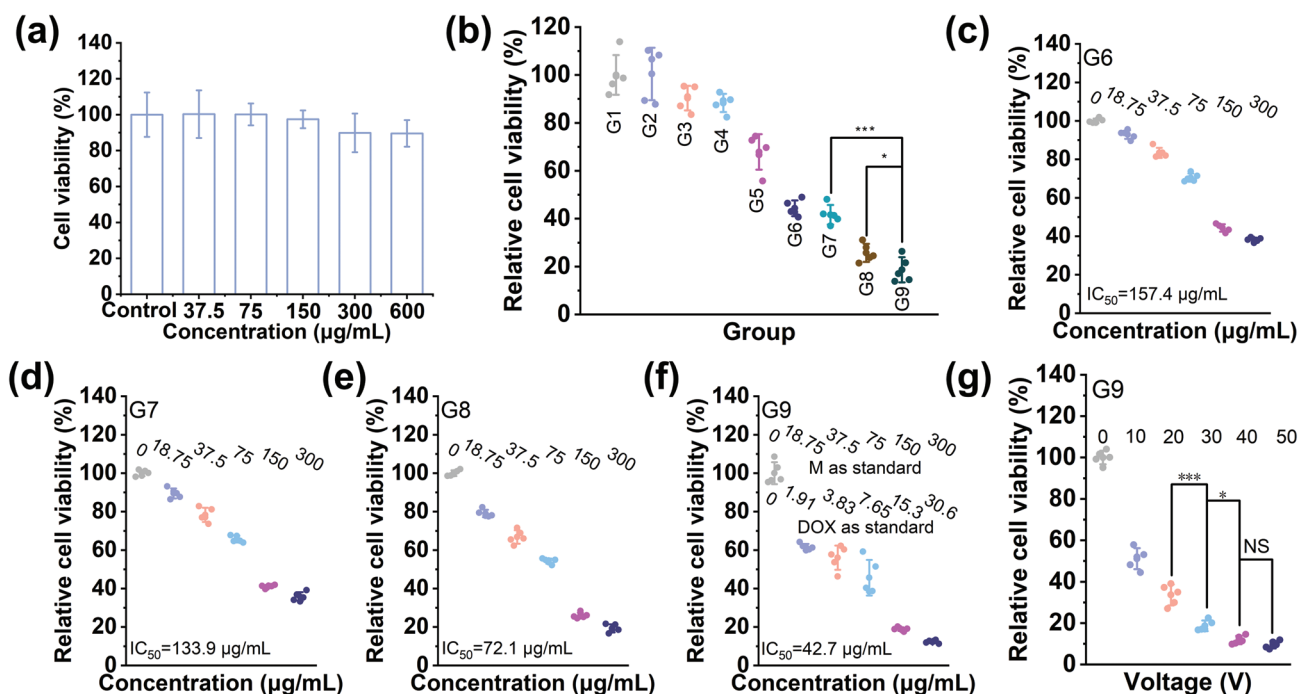


Figure 5. In vitro cancer therapeutic effect of CS-TENG assisted hCOF catalytic system. a) Cell viability of NIH-3T3 cells incubated with different concentrations of hCOF for 24 h. b) Cell viability of 4T1 cells in groups G1–9. G1–9 represent groups of G1 (Control), G2 (E), G3 (H_2O_2 (100×10^{-6} M)), G4 (H_2O_2 +E), G5 (hCOF), G6 (hCOF+ H_2O_2), G7 (hCOF-DOX+ H_2O_2), G8 (hCOF+ H_2O_2 +E) and G9 (hCOF-DOX+ H_2O_2 +E), respectively. (c–f) Cell viability of 4T1 cells in G6–9 at different material concentrations. For group G9, the inset numbers show the corresponding concentration of DOX and hCOF-DOX. (g) Cell viability of 4T1 cells at different voltages of CS-TENG in group G9. Asterisk (*) denotes statistical significance between bars. $p < 0.05$ is considered to be statistically significant conducted using GraphPad Prism 6.0. * represents $p < 0.05$, and *** represents $p < 0.001$ ($n = 5$).

hCOF+ H_2O_2 +E (G8 group) and hCOF-DOX+ H_2O_2 +E (Group G9) groups was mainly due to that the electrical stimulation promoted the release of DOX and the entry of DOX into the cell interior. Meanwhile, the cell killing ability was concentration-dependent in G6–9 (Figure 5c–f). In G9, the cell survival rate was the lowest. When hCOF-DOX concentration was $300 \mu\text{g mL}^{-1}$, the cell survival rate was as low as 10% (Figure 5f). The killing effect in group G9 was voltage-dependent, and the cell survival rate gradually decreased when the applied voltage increased from 0 to 50 V (Figure 5g). At a voltage of 30 V, the cell survival rate was 18.6%. When the applied voltage further increased to 40 and 50 V, the effect of voltage change on cell killing gradually decreased (Figure 5g). The cell viability under 50 V was 9.6%, only 9.1% lower than that under 30 V. The improved cell killing under electrical stimulation was mainly attributed to the following reasons. First, the catalytic performance of hCOF was improved under electrical stimulation. Second, the electrical stimulation also promoted the release of DOX from the nanocarrier, thereby enhancing cell killing.

The results of live and dead staining of 4T1 cells were consistent with that of the cell viability analysis (Figure 6a,d). In the H_2O_2 +E and hCOF-DOX groups, only 29.3% and 36.5% of the cells were dead, respectively. In contrast, in the hCOF-DOX+ H_2O_2 and hCOF-DOX+ H_2O_2 +E, most of the cells (64.5% and 89.9%, respectively) were killed. After the different treatments, intracellular ROS levels were detected using 2,7-dichlorofluorescein diacetate (DCFH-DA) as a ROS indicator. As shown in Figure 6b,e the cells in the hCOF-DOX+ H_2O_2 and

hCOF-DOX+ H_2O_2 +E groups showed increased intracellular ROS levels. The cells in the hCOF-DOX+ H_2O_2 +E group showed the highest fluorescence, with 2.01, 2.46, and 2.78-fold increases compared to the hCOF-DOX, H_2O_2 +E, and control groups, respectively. These results indicated that the electric field stimulation can significantly accelerate the catalytic production of toxic $\cdot\text{OH}$ and elevate cellular ROS.

Since mitochondria are one of the main targets of cellular oxidative damage, we used 5,5',6,6'-tetrachloro-1,1',3,3'-tetraethylimidazolium cyanide (JC-1) as a specific indicator to detect changes in mitochondrial membrane potential (MMP) after the different treatments. JC-1 dye tends to aggregate in normal mitochondria (with red fluorescence), and forms aggregate with green fluorescence when the membrane potential collapses. The cells in the several control groups (control, H_2O_2 , and H_2O_2 +E group) mainly showed red fluorescence, and their green fluorescence signal was almost negligible (Figure 6c,f). In contrast, cells in the hCOF-DOX+ H_2O_2 +E group had the lowest green:red fluorescence ratio, with a 178.5-fold decrease, compared to the control group, suggesting that the cells in the hCOF-DOX+ H_2O_2 +E group had the highest degree of mitochondrial oxidative damage.

We investigated the endocytosis of hCOF and the effect of electric field stimulation on intracellular drug accumulation. Figure 6g,h show that after the incubation of fluorescein isothiocyanate (FITC)-labeled hCOF-DOX (FITC-hCOF-DOX) with the cells for 1 h, red fluorescence of DOX overlapped well with green fluorescence, and no red fluorescence was observed

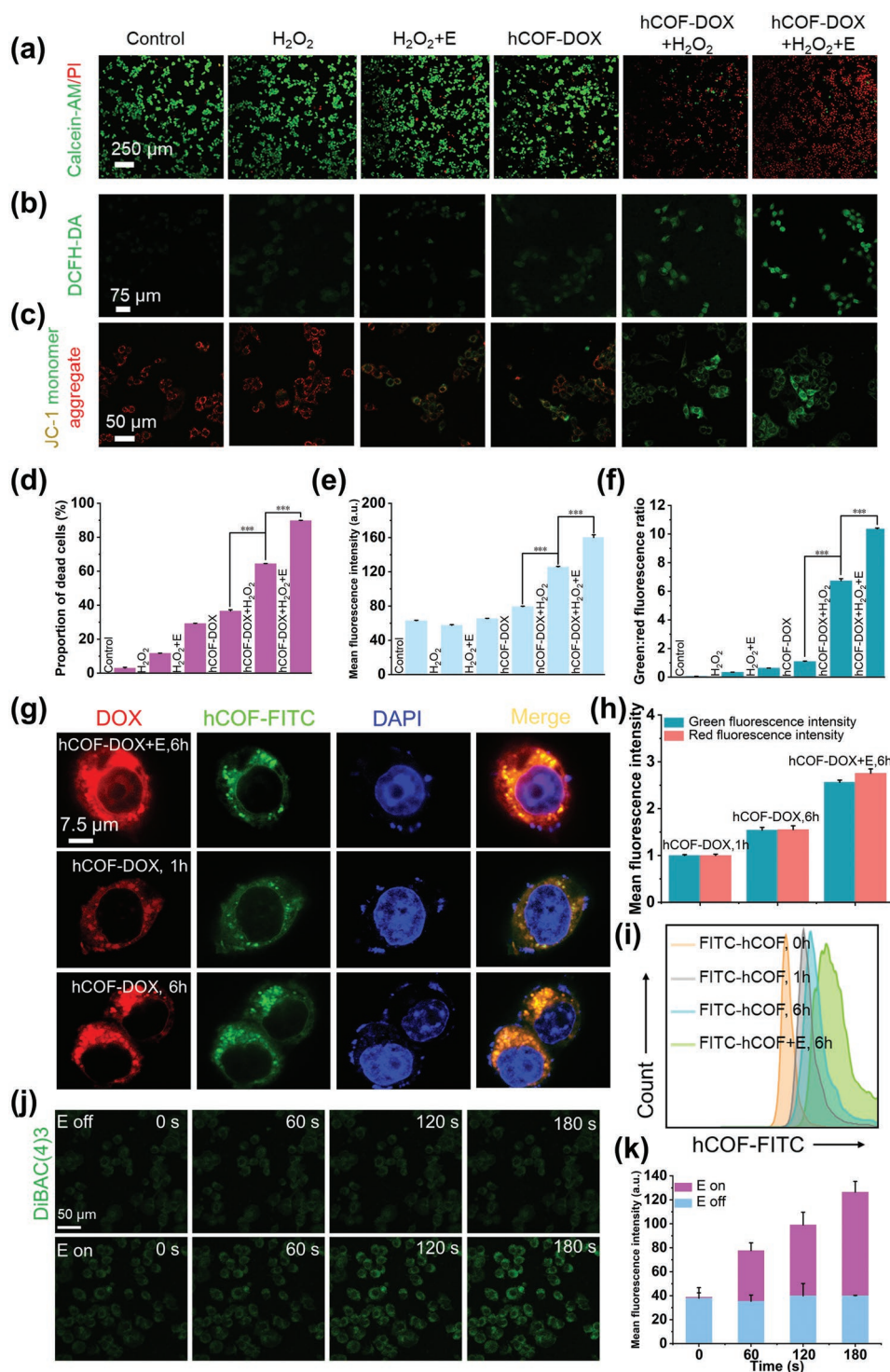


Figure 6. Fluorescent staining results of 4T1 cells. a) Confocal images showing the cells co-stained with Calcein-AM and PI after different treatments. b) Confocal images showing the cells stained with DCFH-DA after different treatments. c) Confocal images showing JC-1 staining of the cells treated with hCOF-DOX and hCOF-DOX+H₂O₂ with or without the electric field stimulation. d) The statistic percentage of dead cells out of the cells co-stained with Calcein-AM and PI. e) The relative fluorescence intensities per cell of the cells stained with DCFH-DA. f) The statistic result shows the relative green:red fluorescence ratio under the different treatments in JC-1 staining. g) Confocal images of the cells after different incubation times of hCOF-DOX, with or without electrical stimulation. The nuclei were stained with 4',6-diamidino-2-phenylindole (DAPI). h) The statistical results show the relative intensity of fluorescence. The average fluorescence intensity of the hCOF-DOX group was set as 1. i) Flow cytometry analysis of the cells treated with FITC-hCOF and FITC-hCOF + E to detect endocytosis of FITC-hCOF into the cells. j) Fluorescence images and k) corresponding statistic results showing the change of plasma membrane permeability during the 180 s electrical stimulation. The cells were stained with DiBAC(4)3. The cells were stained by DiBAC(4)3. Asterisk (*) denotes statistical significance between bars. $p < 0.05$ is considered to be statistically significant conducted using GraphPad Prism 6.0. *** represents $p < 0.001$ ($n = 5$).

in the nucleus, indicating that DOX was not released from hCOF. Further prolongation of the incubation time to 6 h, the yellow fluorescence (overlapped from red and green fluorescence) in the cytoplasm was 1.52 times higher than that at 1 h, indicating further endocytosis of the nanocages into the cells. Finally, under electric field stimulation, the red fluorescence of DOX was distributed throughout the cell, in both cytoplasm and nucleus, indicating that DOX was effectively released from hCOF under the electric field stimulation. The fluorescence intensity of DOX was 1.79 times higher than that without electrical stimulation. Flow cytometry analysis showed similar results to that of fluorescence imaging, implying that the electrical stimulation facilitated endocytosis of hCOF into cells (Figure 6i). To investigate the possible mechanism by which electrical stimulation enhanced the entry of nanoparticles into the cells, the change in cytoplasmic membrane permeability during electrical stimulation was monitored by staining the cells with DiBAC(4)3 as the membrane potential indicator. During the 180 s of electrical stimulation, the fluorescence of the cells increased 3.2-fold compared to that without stimulation. The enhanced membrane permeability can facilitate the entry of nanoparticles into the cells (Figure 6j,k).

2.5. In Vivo Cancer Therapy

With good biocompatibility and anticancer activity in vitro, we further evaluated the therapeutic effect of hCOF-DOX under electrical stimulation against breast cancer in the subcutaneous 4T1 breast cancer model in mice (Figure 7a). First, we verified the biocompatibility of hCOF in vivo. The hemolytic properties of hCOF were tested to characterize the hemocompatibility of hCOF. When the concentration of hCOF was as high as 5 mg mL⁻¹, the hemolysis rate was as low as 2.78% (Figure S15, Supporting Information). Then, different doses of hCOF (12.5, 25, and 50 mg kg⁻¹) were injected into the mice through the tail vein. No clinical abnormality was found during the 14 days of observation. After 14 days, the blood routine indexes, blood biochemical indexes, and tissue H&E histological results of the main organs showed no obvious change compared with those in the control group, demonstrating high biocompatibility (Figures S17 and S18, Supporting Information).

Next, BALB/c mice with subcutaneous 4T1 tumors were randomly divided into 8 groups ($n = 6$), including: 1) control group, 2) E group (local electrical stimulation by CS-TENG), 3) DOX group (intratumoral injection of 102 $\mu\text{g mL}^{-1}$ DOX in PBS), 4) DOX + E group (local electrical stimulation after the intratumoral injection of 102 $\mu\text{g mL}^{-1}$ DOX in PBS), 5) hCOF group (intratumoral injection of 1 mg mL⁻¹ hCOF in PBS), 6) hCOF-DOX group (intratumoral injection of 1 mg mL⁻¹ hCOF-DOX in PBS), 7) hCOF + E (local electrical stimulation after intratumoral injection of 1 mg mL⁻¹ hCOF in PBS), 8) hCOF-DOX+E group (local electrical stimulation after intratumoral injection of 1 mg mL⁻¹ hCOF-DOX in PBS). For exerting electric field stimulation, a flexible CS-TENG was immobilized on the forearm of the volunteer and operated with his fingers at 1.6 Hz for 3 min (electric field intensity of 2.9 V mm⁻¹). The electric field stimulation ($V_{oc} = 30$ V) was delivered to the local tumor tissues by inserting two silver needle

electrodes for moxibustion on the opposite sides of each tumor tissue. After the therapy, the tumor volumes of the mice in the hCOF-DOX+E group were significantly lower than those in the other groups, and the tumor tissues of 3 out of the 6 mice in the group were completely eradicated (Figure 7b–f). The tumor suppression rates of the hCOF-DOX+E, hCOF+E, hCOF-DOX, hCOF, DOX+E, DOX, and E groups were 94.5%, 85.9%, 55%, 49.5%, 38.3%, 31.6%, and 15.8%, respectively. Subsequently, oxidative damage of deoxyribonucleic acid (DNA), proteins, and lipids of the tumor tissues after different treatments were detected (Figure 7g). The results showed significant oxidative damage to DNA, proteins, and lipids of the tumors after treatment with hCOF-DOX and hCOF-DOX +E. The oxidative damage of DNA, protein, and lipids in the hCOF-DOX group were 3.97, 9.45, and 7.38 fold, and those in the hCOF-DOX+E group were 5.41, 13.44, and 12.67 fold of those in the control group, respectively. In contrast, the tumors in the E or DOX+E groups had negligible oxidative damage, further confirming that the catalytically generated ROS caused severe oxidative damage in tumor tissues. Hematoxylin and eosin (H&E) staining results showed obviously reduced malignant cells in both the hCOF-DOX+E and hCOF+E groups (Figure 7h). Ki67 immunohistochemical results also showed minimal tumor cell proliferation in the hCOF-DOX+E group. This superior therapeutic effect was mainly attributed to the increased POD-like activity of the hCOF nanozyme and effective delivery of DOX under the self-powered CS-TENG.

3. Conclusion

In conclusion, we have designed and fabricated a self-driven catalytic promotion system to improve hCOF nanozyme-enabled cancer catalytic therapy. Compared with the conventional way of providing an electric field, the wearable TENG as an electric field simulator has the advantages of self-driven capability without the need for bulky electrical stimulators; high biosafety to reduce unwanted side effects; and flexible modulation. When exerting the electric field on the hCOF nanocage nanozymes with hollow and fully π -conjugated structures, hCOF with intrinsic POD-like activity has enhanced electron migration rate to promote redox reactions during catalytic reactions.

Moreover, the hCOF nanocages can accumulate the electric field energy to the surface of hCOF for augmenting the catalytic redox reaction. At an applied voltage of ≈ 30 V, the POD-like catalytic activity of hCOF increases by 2.44 times, and the increase in voltage can further improve the catalytic activity, which is favorable for the wide voltage range of TENG. The electric field also stimulates the drug release from the hCOF carrier to improve therapeutic outcomes. This work not only optimizes the catalytic energy supply of nanozymes but also provides a new pathway to enhance nanocatalytic disease treatment.

4. Experimental Section

Preparation of COF@ZIF-8: A glass tube was filled with TAPP-Fe (13.5 mg), ZIF-8 (6.25 mg), mesitylene (0.5 mL), and 2,5-Dihydroxyterephthalaldehyde (DHPA, 5.6 mg in 0.5 mL ethanol). Scandium trifluoromethanesulfonate Sc(OTf)₃ (0.1 mL, 4.8 mg mL⁻¹) was then

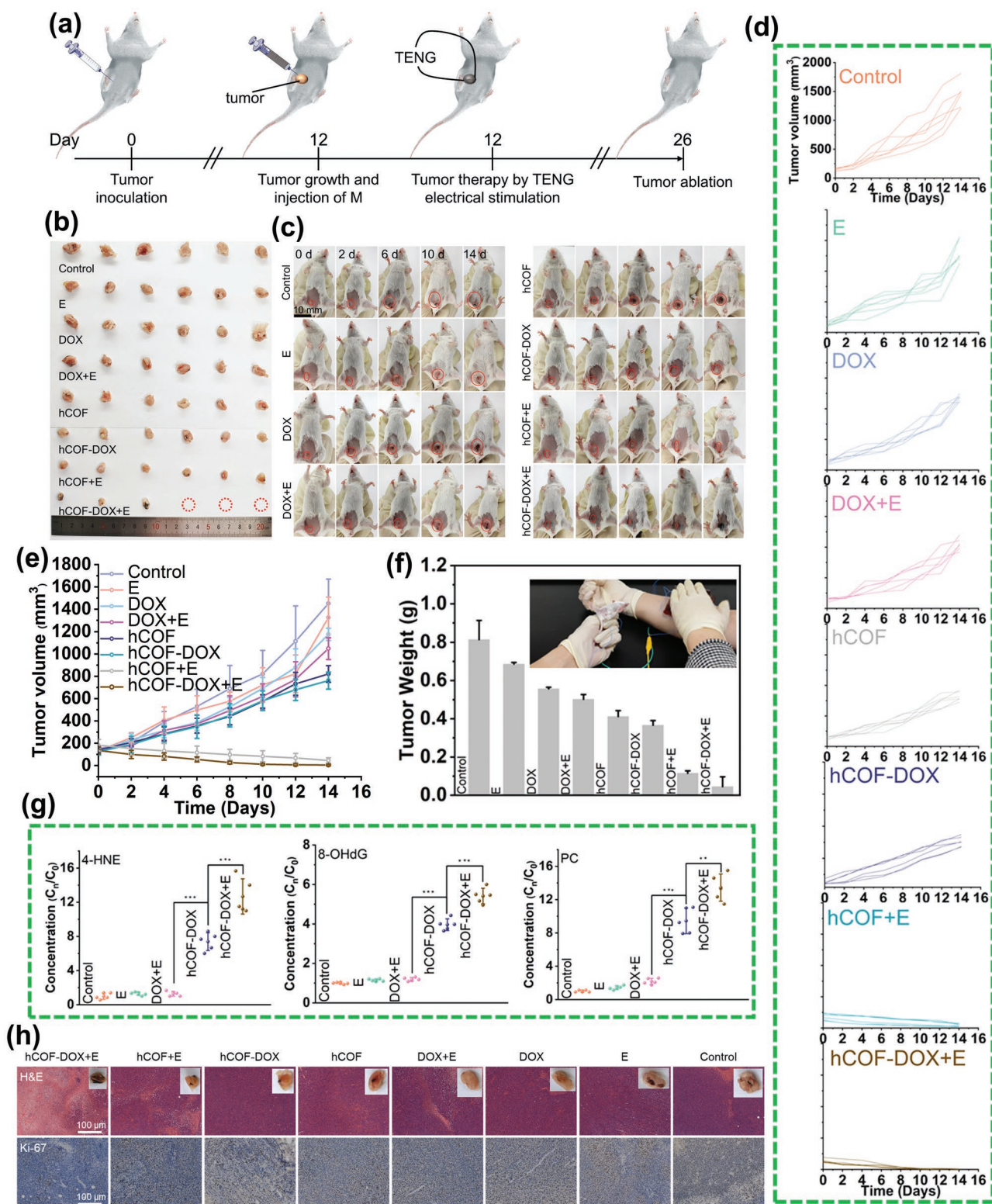


Figure 7. In vivo cancer therapy on the subcutaneous 4T1 tumor-bearing BALB/c mice. a) Schematic illustration of the cancer therapy with the CS-TENG assisted catalytic system. b) Photographs of the stripped tumor tissues at the terminal of the therapy. c) Photographs of the representative mice in different groups during the 14-days of treatment. d,e) Tumor volume change of the mice during the treatment. f) Mean tumor weights after the excision on day 14. The inset is a photograph showing the therapeutic process. g) Changes in 8-hydroxy-20-deoxyguanosine (8-OHdG), protein carbonyl (PCO), and 4-hydroxynonenal (4-HNE) contents after different treatments. h) H&E and Ki-67 staining of the tumor tissues. Asterisk (*) denotes statistical significance between bars. $p < 0.05$ is considered to be statistically significant conducted using GraphPad Prism 6.0. *** represents $p < 0.001$ ($n = 5$).

added to the suspension. The tube was carefully degassed by three freeze–pump–thaw cycles and then sealed under a vacuum. The reaction mixture was sonicated for 60 min. After being thermostated at 70 °C in an oil bath and stirred for 24 h, yellow-brown solid precipitates were obtained. After centrifugation, repeated washing with 1,4-dioxane, tetrahydrofuran, and acetone, and drying at 60 °C under a vacuum for 12 h, the final product of COF@ZIF-8 was collected.

Preparation of hCOF: The as-prepared COF@ZIF-8 (2 mg mL⁻¹) was etched in 50 × 10⁻³ M PB buffer with pH = 5 at room temperature for 1 h. The yellow precipitate was collected by centrifugation and washed with water.

Preparation of hCOF-DOX: 10 mg of hCOF was suspended in 10 mL of DOX aqueous solution at pH = 7. The mixture was placed in a shaker at 37 °C for 24 h, and then the drug-loaded nanocage was washed with water and centrifuged.

Fabrication of CS-TENG: To fabricate the contact-separation mode TENG (CS-TENG), a Cu film (6 × 6 cm) was attached to one end of a Kapton substrate (7 × 16.5 cm), acting as a triboelectric layer and electrode, simultaneously. A layer of PTFE film (6 × 6 cm), acting as the other triboelectric layer, was adhered to the Cu film and then onto the other end of the Kapton substrate with PTFE film facing outside. A foam layer was attached between the Cu film and the Kapton substrate. The device was powered by finger tapping. Informed written consent was signed by all participants driving the TENG.

FITC Labeling for Cellular Endocytosis: To observe cellular uptake, fluorescent FITC was loaded onto hCOF by adsorption. The resulting FITC-hCOF showed a green fluorescence with a fluorescence emission wavelength of 522 nm (λ_{ex} = 488 nm) similar to FITC. Confocal laser scanning microscopy (CLSM) confirmed the uptake of hCOF by the cells. Also, DOX release could be directly observed by CLSM.

In Vivo Cancer Therapy: The in vivo anticancer effect on BALB/c mice with subcutaneous 4T1 tumors was investigated. The animal experiments were approved by the Cancer Hospital, Chinese Academy of Medical Sciences (Approval Number: NCC2021A296). The mice were subcutaneously injected with 4T1 cells (5 × 10⁵ cells suspended in 100 μ L PBS) in the subcutaneous area of the left lower abdomen. When the tumors reached \approx 100–200 mm³ in volume, the mice were randomly divided into eight groups (n = 6): 1) Control group: intratumoral injection of 100 μ L PBS; 2) Electrical stimulation group stimulated by CS-TENG; 3) DOX group with only intratumoral injection of 100 μ L PBS solution containing DOX (102 μ g kg⁻¹); 4) DOX + E group with the electric filed stimulation after the intratumoral injection of 100 μ L PBS solution containing DOX (102 μ g kg⁻¹), 5) hCOF group with only intratumoral injection of 100 μ L PBS solution containing hCOF (1 mg kg⁻¹), 6) hCOF-DOX group with only intratumoral injection of 100 μ L PBS solution containing hCOF-DOX (1 mg kg⁻¹), 7) hCOF + E with the electric filed stimulation after the intratumoral injection of 100 μ L PBS solution containing hCOF (1 mg kg⁻¹), 8) hCOF-DOX+E group with the electric filed stimulation after the intratumoral injection of 100 μ L PBS solution containing hCOF-DOX (1 mg kg⁻¹). Each mouse was earmarked and followed individually throughout the whole experiment. The tumor volume and body weight were recorded during the whole therapeutic course. After 14-days of treatment, the mice were sacrificed and the major organs and tumors were collected for further pathological analysis by H&E staining and Ki-67 immunohistochemistry (for tumor tissues only). All the participants driving the TENG agreed with the experiment.

Immunohistochemistry: Heart, liver, spleen, lung, kidneys, and tumors were fixed in 10% formalin and the fixed tissues were embedded in paraffin, from which continuous 8 μ m sections were prepared. H&E staining was carried out based on the standard protocol. For immunohistochemistry, a Ki-67 monoclonal antibody was used. The images were acquired with an optical microscope.

Statistical Analysis: All data were expressed as Mean \pm SD. error. The statistical difference between different groups of data was evaluated by one-way ANOVA, and p < 0.05 was considered to be statistically significant. Asterisk (*) denotes statistical significance between bars (* p < 0.05, ** p < 0.01, and *** p < 0.001) conducted using GraphPad Prism 6.0.

Supporting Information

Supporting Information is available from the Wiley Online Library or from the author.

Acknowledgements

The work was supported by the National Natural Science Foundation of China (No. 82072065, 81471784), the Strategic Priority Research Program of the Chinese Academy of Sciences (No. XDA16021103), the National Youth Talent Support Program, and the Fundamental Research Funds for the Central Universities (E2EG6802X2).

Conflict of Interest

The authors declare no conflict of interest.

Data Availability Statement

The data that support the findings of this study are available from the corresponding author upon reasonable request.

Keywords

cancer therapies, electron mobilities, nanocages, nanozymes, self-driven electrical stimulations

Received: August 8, 2022
Published online: September 18, 2022

- [1] a) K. Fan, J. Xi, L. Fan, P. Wang, C. Zhu, Y. Tang, X. Xu, M. Liang, B. Jiang, X. Yan, L. Gao, *Nat. Commun.* **2018**, *9*, 1440; b) S. F. Ji, B. Jiang, H. G. Hao, Y. J. Chen, J. C. Dong, Y. Mao, Z. D. Zhang, R. Gao, W. X. Chen, R. F. Zhang, Q. Liang, H. J. Li, S. H. Liu, Y. Wang, Q. H. Zhang, L. Gu, D. M. Duan, M. M. Liang, D. S. Wang, X. Y. Yan, Y. D. Li, *Nat. Catal.* **2021**, *4*, 407.
- [2] a) M. Rojo de la Vega, E. Chapman, D. D. Zhang, *Cancer Cell* **2018**, *34*, 21; b) B. Hassannia, P. Vandenabeele, T. Vanden Berghe, *Cancer Cell* **2019**, *35*, 830.
- [3] a) S. Yao, X. Zhao, X. Wan, X. Wang, T. Huang, J. Zhang, L. Li, *Mater. Horiz.* **2021**, *8*, 3457; b) G. Tang, J. He, J. Liu, X. Yan, K. Fan, *Exploration* **2021**, *1*, 75; c) N. Kumari, S. Kumar, M. Karmacharya, S. Dubbu, T. Kwon, V. Singh, K. H. Chae, A. Kumar, Y. K. Cho, I. S. Lee, *Nano Lett.* **2021**, *21*, 279.
- [4] R. Matheu, E. Gutierrez-Puebla, M. A. Monge, C. S. Diercks, J. Kang, M. S. Prevot, X. Pei, N. Hanikel, B. Zhang, P. Yang, O. M. Yaghi, *J. Am. Chem. Soc.* **2019**, *141*, 17081.
- [5] a) Z. Lian, M. Sakamoto, H. Matsunaga, J. J. M. Vequizo, A. Yamakata, M. Haruta, H. Kurata, W. Ota, T. Sato, T. Teranishi, *Nat. Commun.* **2018**, *9*, 2314; b) J. Li, J. Huang, Y. Lyu, J. Huang, Y. Jiang, C. Xie, K. Pu, *J. Am. Chem. Soc.* **2019**, *141*, 4073; c) Y. Jiang, X. Zhao, J. Huang, J. Li, P. K. Upputuri, H. Sun, X. Han, M. Pramanik, Y. Miao, H. Duan, K. Pu, R. Zhang, *Nat. Commun.* **2020**, *11*, 1857.
- [6] K. Ma, G. Qi, B. Wang, T. Yu, Y. Zhang, H. Li, S. A. Kitte, Y. Jin, *Nano Energy* **2021**, *87*, 106208.
- [7] M. Ge, D. Xu, Z. Chen, C. Wei, Y. Zhang, C. Yang, Y. Chen, H. Lin, J. Shi, *Nano Lett.* **2021**, *21*, 6764.

- [8] X. Ma, X. Ren, X. Guo, C. Fu, Q. Wu, L. Tan, H. Li, W. Zhang, X. Chen, H. Zhong, X. Meng, *Biomaterials* **2019**, *214*, 119223.
- [9] a) T. Chen, T. Gu, L. Cheng, X. Li, G. Han, Z. Liu, *Biomaterials* **2020**, *255*, 120202; b) T. Gu, Y. Wang, Y. Lu, L. Cheng, L. Feng, H. Zhang, X. Li, G. Han, Z. Liu, *Adv. Mater.* **2019**, *31*, 1806803.
- [10] a) S. Shaik, D. Mandal, R. Ramanan, *Nat. Chem.* **2016**, *8*, 1091; b) D. Bim, A. N. Alexandrova, *ACS Catal.* **2021**, *11*, 6534; c) R. C. Fear, S. E. Milan, R. Maggiolo, A. N. Fazakerley, I. Dandouras, S. B. Mende, *Science* **2014**, *346*, 1506.
- [11] F.-R. Fan, Z.-Q. Tian, Z. Lin Wang, *Nano Energy* **2012**, *1*, 328.
- [12] X. Y. Yu, L. Yu, H. B. Wu, X. W. Lou, *Angew. Chem., Int. Ed. Engl.* **2015**, *54*, 5331.
- [13] X. Liang, X. Yu, L. Lv, T. Zhao, S. Luo, S. Yu, R. Sun, C.-P. Wong, P. Zhu, *Nano Energy* **2020**, *68*, 104351.
- [14] a) C. Gao, J. Li, S. Yin, G. Lin, T. Ma, Y. Meng, J. Sun, C. Wang, *Angew. Chem., Int. Ed. Engl.* **2019**, *58*, 9770; b) C. Liu, E. Park, Y. Jin, J. Liu, Y. Yu, W. Zhang, S. Lei, W. Hu, *Angew. Chem., Int. Ed. Engl.* **2018**, *57*, 8984.
- [15] a) T. W. Kim, S. Jun, Y. Ha, R. K. Yadav, A. Kumar, C. Y. Yoo, I. Oh, H. K. Lim, J. W. Shin, R. Ryoo, H. Kim, J. Kim, J. O. Baeg, H. Ihee, *Nat. Commun.* **2019**, *10*, 1873; b) Y. Li, X. Guo, X. Li, M. Zhang, Z. Jia, Y. Deng, Y. Tian, S. Li, L. Ma, *Angew. Chem., Int. Ed. Engl.* **2020**, *59*, 4168.
- [16] M. Li, S. Qiao, Y. Zheng, Y. H. Andaloussi, X. Li, Z. Zhang, A. Li, P. Cheng, S. Ma, Y. Chen, *J. Am. Chem. Soc.* **2020**, *142*, 6675.
- [17] X. Wang, Q. Dong, H. Qiao, Z. Huang, M. T. Saray, G. Zhong, Z. Lin, M. Cui, A. Brozena, M. Hong, Q. Xia, J. Gao, G. Chen, R. Shahbazian-Yassar, D. Wang, L. Hu, *Adv. Mater.* **2020**, *32*, 2002853.
- [18] J. Wang, J. Wan, D. Wang, *Acc. Chem. Res.* **2019**, *52*, 2169.
- [19] L. Wu, H. Zhang, M. Wu, Y. Zhong, X. Liu, Z. Jiao, *Microporous Mesoporous Mater.* **2016**, *228*, 318.
- [20] S. Lin, C. S. Diercks, Y. B. Zhang, N. Kornienko, E. M. Nichols, Y. Zhao, A. R. Paris, D. Kim, P. Yang, O. M. Yaghi, C. J. Chang, *Science* **2015**, *349*, 1208.
- [21] G. Li, W. Hu, Y. Sun, J. Xu, X. Cai, X. Cheng, Y. Zhang, A. Tang, X. Liu, M. Chen, W. Ding, Y. Zhu, *Angew. Chem., Int. Ed. Engl.* **2020**, *59*, 21135.
- [22] a) F. Benyettou, G. Das, A. R. Nair, T. Prakasam, D. B. Shinde, S. K. Sharma, J. Whelan, Y. Lalatonne, H. Traboulsi, R. Pasricha, O. Abdullah, R. Jagannathan, Z. Lai, L. Motte, F. Gandara, K. C. Sadler, A. Trabolsi, *J. Am. Chem. Soc.* **2020**, *142*, 18782; b) G. Zhang, X. Li, Q. Liao, Y. Liu, K. Xi, W. Huang, X. Jia, *Nat. Commun.* **2018**, *9*, 2785.
- [23] a) R. Feiner, L. Engel, S. Fleischer, M. Malki, I. Gal, A. Shapira, Y. Shacham-Diamand, T. Dvir, *Nat. Mater.* **2016**, *15*, 679; b) S. Deng, D. Ma, G. Zhang, N. Yang, *J. Mater. Chem. A* **2021**, *9*, 24472; c) A. Montenegro, C. Dutta, M. Mammetkuliev, H. Shi, B. Hou, D. Bhattacharyya, B. Zhao, S. B. Cronin, A. V. Benderskii, *Nature* **2021**, *594*, 62.